PHYSICAL REVIEW D VOLUME 35, NUMBER 9 1 MAY 1987

Differential cross sections for π^+p and π^-p elastic scattering from 378 to 687 MeV/c

M. E. Sadler
University of California, Los Angeles, California 90024
and Abilene Christian University, Abilene, Texas 79699[*]

W. J. Briscoe,[†] D. H. Fitzgerald,[‡] B. M. K. Nefkens, and C. J. Seftor[†]
University of California, Los Angeles, California 90024

(Received 24 June 1986)

Differential cross sections have been measured for π^+p and π^-p elastic scattering at 378, 408, 427, 471, 509, 547, 586, 625, 657, and 687 MeV/c in the angular range $-0.8<\cos\theta_{\text{c.m.}}<0.8$. The scattered pion and recoil proton were detected in coincidence using scintillation-counter hodoscopes. A liquid-hydrogen target was used except for measurements at forward angles, in which a CH_2 target was used. Statistical uncertainties in the data are typically less than 1%. Systematic uncertainties in acceptance and detection efficiency are estimated to be 1%. Absolute normalization uncertainties are 2–3 % for most of the data. The measurements are compared with previous data and with the results of recent partial-wave analyses. The data are fit with Legendre expansions from which total elastic cross sections are obtained.

I. INTRODUCTION

The simple spin and isospin structure of the pion-nucleon system makes it a unique source of information on the hadronic interaction. The πN scattering amplitudes have been determined accurately from 200–400 MeV/c, where the P_{33} resonance dominates. At higher momenta the determination is not as accurate, due to the overlapping resonances, their increasing widths, the opening of inelastic channels, and the fact that complete data sets of high precision have been lacking.

In the absence of a dynamical theory for the πN interaction, data of high accuracy are required to determine the scattering amplitudes, to search for possible new resonances, and to determine masses and widths off resonances. The latter are important for testing strong-interaction models, such as the Isgur-Karl quark model,[1] hybrid models,[2] and Skyrmion models.[3]

It is desirable to test the validity of isospin invariance over a broad range of beam energies and momentum transfers. QCD and quark models predict a small violation of isospin invariance as a consequence of the mass difference between the up and down quarks.[4] This small isospin violation is a fundamental property of the strong interactions, different from the well-established electromagnetic isospin breaking. A model-independent test of isospin invariance consists of checking the triangle inequality

$$\tfrac{1}{2}[(\sigma^+)^{1/2}-(\sigma^-)^{1/2}]^2<\sigma^0<\tfrac{1}{2}[(\sigma^+)^{1/2}+(\sigma^-)^{1/2}]^2 , \quad (1)$$

where $\sigma^{\pm},\sigma^0$ are the differential cross sections for $\pi^{\pm}p\rightarrow\pi^{\pm}p$ and $\pi^-p\rightarrow\pi^0n$ (charge exchange), respectively. Relation (1) must be satisfied at every energy for all angles for the differential cross sections measured with an unpolarized target as well as for the transversity cross sections. (The transversity cross sections are the cross sections measured using a transversely polarized target.) A violation of the triangle inequality for transversity cross sections was recently reported.[5] Although preliminary results by our group do not support this conclusion,[6] it still warrants further investigation.

New developments in QCD have resulted in the proposal that a new type of hadronic matter should exist called hybrid matter.[2,7] It consists of quarks plus one or more constituent gluons. Simple bag-model calculations[8,9] suggest that the lowest-mass hybrid is around 1400 MeV; it could thus form a double hump with the $P_{11}(1440)$ resonance.

The properties of the $P_{11}(1440)$, or Roper, resonance, summarized in Table I, are not known with precision. The Saclay group[14] was the first to propose a double P_{11} resonance. A Russian analysis[15] and the recent analysis by the VPI group[16] also contain two P_{11} resonances in this energy region. The latter report the location of two poles in the complex plane at (1359, $-100i$) and (1410, $-80i$) MeV.

TABLE I. Properties of the $P_{11}(1440)$ resonance as given by different partial-wave analyses.

PWA	Mass (MeV)	Width (MeV)	Elasticity	Reference
Karlsruhe	1410±12	135±10	0.51±0.05	10
CMU-LBL	1440±30	340±70	0.68±0.04	11
Glasgow	1411	344		12
Baker	1472	113		13
Saclay	1413,1532			14

An interesting recent development has been the emergence of the Skyrmion[3] model. Besides detailed predictions of the Argand plots of all πN scattering amplitudes this model gives novel relations between the isospin $\frac{1}{2}$ and $\frac{3}{2}$ amplitudes.

Many subtle variations on the standard bag model for quark confinement in hadrons have been investigated in the last several years. Various models can be tested through their πN resonance parameter predictions. A typical example of this is the perturbed-harmonic-oscillator quark model by Celmaster,[17] in which a new S_{11} resonance of mass 1335 ± 65 MeV is predicted.

Evidence has been reported recently[18] for a new, very narrow (~ 16 MeV) dibaryon resonance with a mass of 2.24 GeV. This possible discovery is spurring new searches for very narrow πN states that could have been overlooked in previous experiments.

The results reported here are absolute differential cross sections for $\pi^\pm p \to \pi^\pm p$ at $P_\pi = 378$, 408, 427, 471, 509, 547, 586, 625, 657, and 687 MeV/c. They comprise one part of a program designed to produce a complete set of measurements of $d\sigma/d\Omega$, A_N, A, and R, all at precisely the same incident momentum. The measurements at lower momenta overlap with existing data in the region of the first resonance while the measurements at higher momenta lie in the region of the second resonance and the threshold for $\pi^- p \to \eta n$.

II. EXPERIMENTAL SETUP

A. Beam and beam monitors

The experiment was performed in P^{3}E, the east leg of the pion and particle physics channel of the Clinton P. Anderson Meson Physics Facility at the Los Alamos National Laboratory[19,20] (LAMPF). The channel views a carbon production target at 20° with respect to the primary 800-MeV proton beam. Three dipoles provide momentum selection, momentum dispersion for selecting the momentum bite, and switching to either the east or west experimental areas. Focusing is accomplished by six quadrupole doublets and the beam phase space is controlled by two horizontal and two vertical slits. A more complete description of the P^3 channel, including tuning procedures, momentum determination, and contamination measurements, has been previously reported.[21]

The accelerator duty factor was 7.4% with a 620-μsec beam spill. The spill had a microstructure of 5-nsec intervals between beam bursts. The pion beam rates were limited so that the dead time in the data acquisition was less than 4% at lower momenta. At higher momenta the limiting factor was the momentum acceptance, which never exceeded $\Delta P/P = 1\%$.

The horizontal and vertical spatial distributions of the beam were determined by remotely controlled scanning counters, shown as X and Y in Fig. 1. These counters were 0.6 cm wide and were positioned 1.7 m downstream of the target. Alignment was checked by producing a waist in the beam at the scanning counters, then changing the last four quadrupoles to produce a waist at the target and again measuring the beam position at the scanning counters. The fields in the last two bending magnets were adjusted in an iterative fashion until the beam was centered at the scanning counters with both waist positions, verifying that the beam was not being steered by the quadrupoles.

The transverse spatial distributions of the beam could be described reasonably well by Gaussians at the waist positions, with nominal horizontal and vertical widths of 1.5 and 2.0 cm [(FWHM) full width at half maximum], respectively. These widths and the variation of the widths with waist positions at different locations were consistent with the calculated beam phase space as modeled by the computer program TURTLE (Ref. 22). The horizontal and vertical beam divergences as calculated by TURTLE were nominally 10 and 20 mrad (FWHM), respectively.

Because of the poor reproducibility of the beam-contamination measurements in the special beam-tune runs,[21] the contaminations were monitored on line using time-of-flight (TOF) and Cherenkov-counter techniques. The on-line TOF measurements were accomplished by chopping the primary proton beam so that every tenth macropulse had a microstructure of 1 μsec between beam bursts. This time structure was adequate for timing the arrival of particles at the beam counters (labeled S_1 and S_2 in Fig. 1) with respect to the chopper frequency. Different particle species could then be identified by the TOF differences in traversing the distance from the production target to the beam counters.

The chopped beam was not always available during the experiment due to malfunctioning of the chopper mechanism and constraints of other experiments running concurrently. In particular, no chopped beam was available for the π^+ measurements at 657 and 687 MeV/c. Consequently, there is a larger normalization uncertainty for these momenta due to the large proton contamination (~ 60–70% at 687 MeV/c).

The Cherenkov counter (C in Fig. 1) was 1 m long and filled with isobutane gas at atmospheric pressure. A thin mirror at the downstream end reflected the light from the Cherenkov cone vertically upward where it was detected by a 12-cm photomultiplier tube. The isobutane was bubbled continuously through the detector into the atmosphere. The Cherenkov counter was sensitive only to the electrons in the beam. The efficiency for electrons was 97% and the rejection for pions was better than 1:1000.

Two muon telescopes (designated M_1 and M_2 in Fig. 1) were situated 2.5 m downstream from the target and were used in the beam normalization. They were calibrated at low rate using the beam counters S_1 and S_2 and were

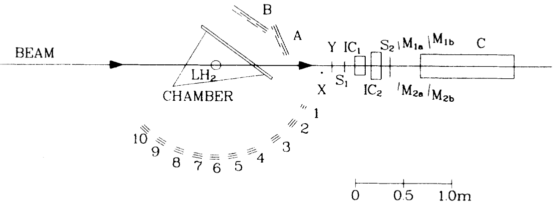

FIG. 1. Layout of the experiment.

TABLE II. Beam momentum bite, contaminations, and intensities.

P (MeV/c)	$\pi^{+/-}$	$\Delta P/P$ (%)	% e	% μ[a]	% p	Rate (10^6 π/sec)
378	π^+	0.8	0.7—1.3	1.8	0.1	0.2—6
408	π^+	0.4	0.4	1.4	0.5—1.6	0.2—6
427	π^+	0.4	0.3	1.3	1.1—1.7	0.2—5
471	π^+	0.4	0.1	0.9	0.4—2.0	0.4—1
509	π^+	0.4	0.07	0.7	0.8—10.2	0.3—5
547	π^+	0.4	0.05	0.5	1.4—2.8	0.3—5
586	π^+	0.4	0.03	0.4	2.2—8.3	0.7—6
625	π^+	0.5	0.02	0.3	8.0—30.	0.7—3
657	π^+	1.0	0.02	0.2	21.0—30.0	0.5—2
687	π^+	1.0	0.01	0.2	69.0—74.0	0.5—2
378	π^-	0.8	6.7	1.8		2.5—16
408	π^-	0.4	5.7	1.4		2—13
427	π^-	0.4	3.7	1.3		2—11
471	π^-	0.5	2.9	0.9		2—11
509	π^-	0.5	1.7	0.7		2—9
547	π^-	0.4	1.4	0.5		2—6
586	π^-	0.7	1.1	0.4		1—9
625	π^-	0.7	0.7	0.3		2—7
657	π^-	1.0	0.5	0.2		0.7—3
687	π^-	1.0	0.5	0.2		0.5—1

[a] These are "on-momentum" muons only. Decay muons are treated in the two-meter correction described in the text.

used to determine the rate response of the beam counters. Two ionization chambers, IC_1 and IC_2 in Fig. 1, provided additional monitoring of the beam flux.

The central beam momentum was known to 0.3% (Ref. 17). The momentum bite, electron, muon, and proton contaminations, and range of beam rates used in the measurements are given in Table II.

B. Targets

The main target used in the experiment was liquid hydrogen (LH_2). The target flask was a vertical cylinder with a height of 19.1 cm and a diameter of 10.16±0.05 cm. The flask wall consisted of 0.25 mm of Mylar; the flask was wrapped with 10 layers of 0.006-mm aluminized Mylar for insulation. Independent measurements with a 12.70±0.05 cm target were made at 408 (π^+ and π^-), 427 (π^-), and 625 MeV/c (π^-). The thickness of the LH_2 targets was sufficient to stop the recoil protons from forward-angle pion scattering, thus precluding coincidence measurements at these angles. A thin (0.127 cm) CH_2 target was used in forward-angle pion scattering measurements in order to provide uniform angular coverage up to $\cos\theta_{\text{c.m.}} \sim 0.8$. The background subtraction was substantially larger for CH_2 than for LH_2, particularly at scattering angles where the elastic cross sections are low. For this reason the CH_2 target was used only at forward angles, where the cross sections are relatively large, and for consistency checks.

The LH_2 target was operated at an absolute pressure of 13.4±0.2 psi, which corresponds to a density of 0.071 15±0.000 05 g/cm^3 at the boiling point. The target was emptied for background measurements by closing off a valve through which the hydrogen gas was returned to the refrigeration system. This action forced the liquid into a reservoir as it was displaced by the gas. The "empty" target thus contained saturated hydrogen gas at the same pressure, corresponding to a density of 0.001 29±0.000 06 g/cm^3. Since the yields for the background runs were subtracted from the yields for the production runs, the effective density was taken as the difference, or 0.069 86±0.000 08 g/cm^3.

The target diameter was measured with calipers at differential pressures of 0—30 psi at temperatures down to that of liquid nitrogen. The net change in target diameter due to the combined effect of increased pressure and lower temperature was less than 0.5%, obtained by extrapolating the measurements at liquid-nitrogen temperature to LH_2 temperature.

The correction for bubbles in LH_2 depends on the boiling rate and the terminal velocity of the bubbles. The boiling rate was evaluated by measuring the time (7 min) it took to empty the target, using carbon resistors placed near the top and bottom of the cylinder which sensed a temperature change when exposed to the warmer hydrogen gas. The bubble velocity was estimated to be 16±4 cm/sec for bubbles ranging in size from 0.3 to 3 mm, based on the viscosity and density of LH_2. A detailed discussion of the procedures is given in Ref. 23. The overall correction was 0.5±0.2%.

C. Detectors

Twelve hodoscopes containing a total of 48 scintillation counters were used to detect the scattered pions and recoil protons in coincidence. The floor layout of the detectors is shown in Fig. 1. Ten pion arrays were situated 100 cm from the target center at laboratory angles of 26.7°, 38.7°, 52.5°, 68.5°, 80.0°, 90.6°, 100.6°, 111.7°, 123.8°, and 135.8°. The solid angles, 10 msr for the first pion array and 30 msr for the other nine, were determined by the front (F) counter. The F counter was 5 cm wide, 20 cm high, and 0.3 cm thick for the first array, and 10 cm × 30 cm × 0.3 cm for the other arrays. Behind the front counter were an up (U) and a down (D) counter which were 11 cm × 21 cm × 0.6 cm (6 cm × 14 cm × 0.6 cm for array 1). These counters divided each array into upper, middle, and lower regions defined by the triggering combinations $FU\bar{D}$, FUD, and $F\bar{U}D$, respectively, where the overbar represents an anticoincidence.

Two proton arrays (labeled A and B in Fig. 1) were situated at 70 and 60 cm from the target at angles of 22.6° and 53.5°, respectively. The choice of the geometry of the proton counters was based on a Monte Carlo simulation of elastic scattering that incorporated the geometry of the pion arrays and of the targets as well as the beam-spot size, divergence, and momentum bite. Each array had five vertical counters, 0.3 cm thick, which defined the scattering angle. The end counters on the forward proton array and the most-forward counter on the back proton array were 5 cm wide. The remaining counters were 15 cm wide and overlapped with adjacent counters to define 5-cm-wide regions using the triggering combinations. These regions corresponded to an angular acceptance of 4°–5° for the recoil protons. The protons incident on the most backward counter often had insufficient energy to traverse two layers of scintillator so the last region (numbered 15) was actually 10 cm wide and was defined by the most backward counter triggering without the overlapping counter. Region 14 was defined by the last two counters triggering together, region 13 by the next-to-last counter triggering by itself, and so on, to region 1 which was defined by the two most forward counters triggering simultaneously. The heights of these counters ranged from 18 cm for the most forward counter on the forward array to 50 cm for the most backward counter on the back array.

The four horizontal counters used to determine coplanarity for each of the proton arrays overlapped slightly and were tapered (narrower for the more forward protons). Coplanarity of the two-body final state required one of the following: (1) a pion to pass through the upper region of a pion array ($FU\bar{D}$) and a proton to pass through one of the two lower horizontal counters, (2) a pion to pass through the middle region of a pion array (FUD) and a proton to pass through the middle two horizontal counters, or (3) a pion to pass through the lower pion region ($F\bar{U}D$) and a proton to pass through one of the two upper horizontal counters.

The use of counter hodoscopes had the advantages that full angular coverage was obtained without moving the apparatus, the uncertainty of determining the acceptance was minimized, and corrections for in-flight pion decay were easily made.

III. ANALYSIS

A. Replay and cuts

The event trigger determined by the experimental electronics was a very relaxed one so that good events were actually selected by software cuts in the off-line analysis and not in the hardware. A trigger was generated by a coincidence of pion arrays 1–6 with any one of the vertical counters in the backward proton array or pion arrays 4–10 with any one of the vertical counters in the forward proton array. For each valid trigger, the information recorded on magnetic tape for use in off-line analysis consisted of the following.

(1) Pulse heights in the pion counters.

(2) Pulse heights in the proton counters. The combination of pulse-height information from both the pion and proton arms was sufficient to reject unambiguously unwanted events such as reverse elastics (protons going into pion counters and vice versa), even at the highest beam momentum measured.

(3) Vertical counter latches for kinematics. The 10 overlapping vertical proton counters divide the proton arrays into 15 regions, defined by the triggering combinations, which yielded an angular resolution of 4.2° and 4.9° for the back and front proton arrays, respectively.

(4) Horizontal counter latches for coplanarity. Cuts based on coplanarity yielded another determination of the nonelastic background which is significant at the higher momenta.

(5) Time of flight (TOF). This signal provided the best single determination of the elastic events.

A background subtraction was performed after all the cuts had been applied. For runs with a LH_2 target, the background spectra were determined by running with an empty target; the spectra were analyzed with the same cut values as for the production run. This background-to-signal ratio was typically a few percent but was as high as 30% for the low cross sections at the higher momenta for π^+. This background came primarily from scattering in the target walls. For the runs with the CH_2 target, the background was measured using a carbon target whose thickness was chosen to give the same energy loss for the beam. This correction was 5–15 % at the forward angles where the CH_2 analysis was most important, and was as much as 50% for the lowest cross sections (pion array 6 at the higher momenta).

At the most forward scattering angles (pion arrays 1 and 2 below 427 MeV/c, array 1 at or above 427 MeV/c), the recoil protons had enough energy to escape from the CH_2 target but did not have enough energy to reach the second plane of the proton array. Because coplanarity was determined in this plane the coplanarity cut could not be applied and a different technique was used for the background subtraction as follows. The background was described by two free parameters which were determined by fitting. The parameters were a normalization and a constant applied to the cross sections from the CH_2 analysis. The normalization was an overall multiplication factor applied to each array and the constant was subtracted from each array. These parameters were varied to obtain the best fit to the cross sections from the LH_2 analysis at arrays 3–6, where the CH_2 and LH_2 measurements overlapped. The results from this technique were compared to those from the standard CH_2 analysis (using the coplanarity cut) and were found to be consistent within the uncertainties of the data. The constant and normalization were then applied to the forward-angle arrays. Although such a fit is empirical, it is not without physical justification. The technique was motivated by the assumption that the background from the carbon was due primarily to quasielastic scattering of the incident pions by the bound nucleons in carbon and would therefore have an angular distribution similar to the πp events. If this were strictly true only the normalization term would be needed. The constant term allowed the fit some freedom to account for a smearing of the πp angular distribution which is expected because of the Fermi motion of the bound nucleons. At the lower momenta the correction amounted to less than 1% of the cross section at the first pion array for the π^+ beam and 5–6% for the π^- beam.

B. Beam normalization and dead times

The number of pions in the beam was determined by direct counting. Two scintillation counters (labeled S_1 and S_2 in Fig. 1) were placed in the beam 1.5 and 2 m downstream of the target and the coincidence rate was determined.

Corrections made to the number of coincidence counts were as follows.

(1) Electron contamination as determined by the Cherenkov counter. The electron contamination originates from π^0's created in the internal production target when the decay γ's convert into electrons. A linear dependence of the amount of this contamination on the position of the primary proton beam on the production target is expected and was observed.

(2) Proton contamination of the π^+ beam. It has been noted previously[21] that there is a sizable variation of the proton contamination with the position of the primary proton beam on the production target. Reduction of the proton contamination of positive beams is accomplished in the P^3 channel by the degrader method. A carbon degrader inserted at an intermediate focus produces a momentum separation of pions and protons; the second dipole translates this into a spatial separation at the position of the proton absorber (a moveable jaw). The position of the proton absorber is adjusted to give the optimum π/p ratio.

(3) Muon contamination. This contamination (for on-momentum muons, i.e., muons which originated near the production target) was determined by range measurements using copper and were reported previously.[21] The contaminations are listed in Table II for each of the beams.

(4) The dead time of the counter coincidence between S_1 and S_2. Typical dead-time corrections were 2–6% for the beam rates used with the liquid-hydrogen target and were determined in conjunction with the sagging of the counters as discussed in the next paragraph.

(5) Sagging of the phototubes of the beam counters S_1 and S_2 at high beam rate. The inefficiency of the counters due to the sagging was negligible at the rates used in the production runs with the LH_2 target but was significant for the beam rates used with the CH_2 target. The amount of sagging was determined using the two muon decay telescopes. For each production run a set of calibration runs was made by varying the beam rate from $10^4\pi$'s/sec to a rate approximately twice that used in the production run when possible. The ratio of the number of counts in the $S_1 \cdot S_2$ coincidence to the sum of the counts in the muon telescope coincidences decreased with increasing beam rate. An empirical calibration factor F_C was determined by fitting a curve through these points. The function which was fit was

$$F_C(r) = \alpha e^{r\tau}[1+\beta(r\tau)^\gamma] , \tag{2}$$

where α, β, γ, and τ were fit parameters and r is the beam rate. The parameter τ is the dead time in the $S_1 \cdot S_2$ coincidence. The exponential factor corrects for this dead time and the term in square brackets describes the sagging at high rate. This function was found by inspection and gave excellent fits to the response of $S_1 \cdot S_2$ over the wide range of rates in the calibration runs. In the limit $r \to 0$, $F_C(0) = \alpha$. For a particular run the number of events in the $S_1 \cdot S_2$ coincidence was multiplied by $F_C(r)/\alpha$ to obtain the true beam rate. For production runs at high rates the number of beam particles was determined by multiplying the counts in the muon counters by α. The reproducibility in determining α was found to be 2–5% using independent calibration runs taken before and after the production run. Therefore, the beam rates were kept low so that only a small correction was needed for $S_1 \cdot S_2$. This correction was typically 2–10% for runs with the LH_2 target but was much larger for runs with a CH_2 target (from 30% up to a factor of 3). For this reason, the CH_2 runs were normalized to the LH_2 runs at angles where the analyses overlapped (nominally counters 2–6).

(6) Pion decay in the 2-m flight path between the last quadrupole of the channel and the target and the 1.4 m between the target and the beam counters. This "two-meter correction" was obtained using a Monte Carlo simulation which traced the beam pions and the decay muons from the last quadrupole to the beam counters downstream of the target. The two-meter correction is the ratio of the number of pions at the target center divided by the total number of particles (pions plus decay muons) which were incident on the beam counters. This correction varied from 1.004 at 378 MeV/c to 0.979 at 687 MeV/c. Ratios lower than 1 are possible since muons which originate from pion decay before the target may still be incident on the beam counters.

(7) Dead time of the electronics for data acquisition. When a trigger (T) was generated a busy signal was fed back in anticoincidence ($\bar{B}$) to the gating electronics to inhibit subsequent triggers while the analog-to-digital converters (ADC's) and time-to-digital converters (TDC's) were digitizing and being read. This interval was 200 μsec. The number of triggers recorded on tape was then the number of occurrences of $T \cdot \bar{B}$. The dead time was monitored by fast electronics (limited only by the 40-nsec coincidence width) which scaled the number of triggers regardless of whether the electronics was busy. The live time was then derived from $T \cdot \bar{B}/T$. Beam rates were adjusted so that the dead time was 2–4% except for special runs which were taken at higher rate to test the validity of this dead-time correction. At the rates for the production runs the dead time associated with the 40-nsec-fast coincidence is negligible ($<0.001\%$).

C. Monte Carlo calculation

A Monte Carlo simulation was used to evaluate corrections for (1) the effect of the finite beam size and its overlap with the cylindrical targets, (2) the decay of the scattered pions, (3) the deflection and energy loss caused by multiple Coulomb scattering of the outgoing particles, (4) the attenuation of pions and protons due to hadronic processes as they traversed the target medium, (5) the finite acceptance in scattering angle of the detectors, and (6) the effect of the kinematic and coplanarity cuts used in the analysis.

Each simulated beam particle was randomly selected from the input distributions of the momentum bite, the beam spot at the focus, and the angular divergence. The momentum distribution was uniform and the spatial and angular distributions were Gaussian. An interaction point in the target was selected along the trajectory. The cosine of the center-of-mass scattering angle, $\cos\theta_{\text{c.m.}}$, was weighted using an input angular distribution parametrized from a polynomial expansion of the form

$$\frac{d\sigma}{d\Omega}=\sum_{i=0}^{n} a_i \cos^i\theta_{\text{c.m.}} \ , \tag{3}$$

where n was 4 or 5, depending on the momentum. The outgoing particles were then propagated through the target and their energy loss and deflection due to multiple scattering were calculated using the subroutine ELOSS (Ref. 24). These trajectories were then extrapolated to the detectors to see which, if any, of the detectors were hit. Pion decay into a muon and a neutrino was incorporated using an exponentially weighted random-number generator. If the decay occurred before the pion passed the detector plane, the muon's trajectory was calculated using a uniform distribution in the π rest frame and this vector was transformed into the laboratory frame.

A running average of the distance traveled by the beam particles in the target was stored for all events in which the scattered pion or muon trajectories intercepted a pion array. The mean and standard deviation of the following quantities were also tabulated individually for events which produced a particle in the pion arrays: scattering angle, distance in the target traversed by the pion and proton, and the average momenta of the outgoing particles.

Considering only the decay muon trajectories and the pion detector geometry, there was an almost equal number of pions that (a) would have been incident on a particular array but decayed to muons that missed, compared to (b) the number of muons which hit the same array that arose from pions that would have missed. This cancellation became less exact as the cuts on kinematics and coplanarity were imposed. The fraction of rejected events in the Monte Carlo program was less than 1% of the total. The effect was doubled when the event failed the coplanarity cut (the last one applied) since these failures were used as an estimate of the background subtraction. Improper accounting of these events as background would cause a subtraction from the yield of valid πp events. These events are quite different from ordinary background events (due to inelastic processes, scattering from the target walls for LH_2, and quasielastic scattering from the carbon in CH_2).

The number of πp events which failed the ordinary coplanarity cut was strongly dependent (at the few per cent level) on the assumed beam phase space. As described earlier, the spatial distribution was determined by using the scanning counters and the divergence was obtained from TURTLE (Ref. 22). The situation was worse for the forward-going protons (back-angle pions), yielding corrections as large as 7% for some of the beams. These failures were evident for the latter runs during which a vertical slit (MSO2) was stuck in the out position. These runs were analyzed with a relaxed coplanarity cut, defined so that only events which were two regions away from on coplanar were rejected. The number of events that failed this cut was then multipled by five to account for solid-angle matching and subtracted from the yield.

Corrections for the absorption of outgoing particles due to a secondary hadronic interaction were evaluated in the following manner. The average path lengths x_{avg} and momenta of scattered particles were obtained from the Monte Carlo simulation. The total cross sections σ_t for πp and pp scattering (and for πC and pC scattering when using a CH_2 target) were obtained from the VPI phase-shift analyses[16] and from the literature. The factor $\exp(-n\sigma_t x_{\text{avg}})$, where n is the hydrogen or carbon density, was then used for the absorption. This correction was as large as 4% in the π^+ analysis for angles where the outgoing pion had a momentum near 300 MeV/c, and 2% for counters 1 and 2 with the CH_2 target. The CH_2 target was oriented with the tangent to the target face directed at 33° in the laboratory, between arrays 1 and 2, to minimize the energy loss of the recoil protons. The average path lengths of the scattered pions in the CH_2 were about 0.8 cm. The total cross sections were used for these corrections with no compensation for particles which scatter at small angles and still satisfy the applied cuts. This approach was used because of the way the background was subtracted. Particles which scatter at small angles, yet just enough to miss the coplanarity cut, would cause the event to be subtracted as background in the analysis. Interactions in the air between the scattering chamber and the detectors were neglected since the nuclear collision length for air is ~ 80 times that for LH_2.

The correction for the effective target length ranged from 1% to 3%, being larger for the higher momentum beams where more of the channel acceptance was utilized. The total correction for the other effects described above ranged from 2% to 5% with a nominal value of 3%. The uncertainties associated with the corrections were taken to be 20% of the total. The attenuation factor for incident pions in the target and its uncertainty were evaluated in like manner. The "Monte Carlo correction factor" was taken as the ratio of these factors with the uncertainties added in quadrature.

The solid angles in the center-of-mass frame $\Delta\Omega_{\text{c.m.}}$ of the pion arrays were also obtained using the Monte Carlo program. The number of pions and associated decay muons which were incident on each array were counted assuming a uniform angular distribution. This number, multiplied by 4π and divided by the total "number of throws," gives $\Delta\Omega_{\text{c.m.}}$. Enough hits were accumulated for each array to determine the solid angle to within a statistical uncertainty of ±0.2%. This technique incorporated the full geometry of the detectors and targets as well as the beam phase space in the determination of the acceptance.

A correction was applied to account for the finite angular acceptance of the pion detectors. The acceptance of a given pion array as a function of $\cos\theta_{\text{c.m.}}$ was determined to be approximately Gaussian from the Monte Carlo program which modeled the experiment. This Gaussian shape is a result of the combined effects of the detector size, the target interaction volume, and the beam phase space. Using a uniform scattering distribution in the Monte Carlo simulation, the centroid μ_j, and standard deviation σ_j of the acceptance interval for pions incident on the jth array were determined. A computer program GAUFAC was written to determine the Gaussian-weighted finite-acceptance correction. The program performed a least-squares fit to the angular distribution by varying the parameters a_i in

$$\frac{d\sigma(x)}{d\Omega}=\sum_{i=0}^{n} a_i x^i , \tag{3'}$$

where $x=\cos\theta_{\text{c.m.}}$ to minimize χ^2 defined by

$$\chi^2=\frac{1}{m-n-1}\sum_{j=1}^{m}\frac{\left[\frac{d\sigma(x_j)_{\text{int}}}{d\Omega}-\frac{d\sigma(x_j)_{\text{expt}}}{d\Omega}\right]^2}{(\delta\sigma_j)^2} . \tag{4}$$

The sum is over the m pion arrays (9 at 378 MeV/c, 10 for all other momenta). The $d\sigma(x_j)_{\text{expt}}/d\Omega$ are the uncorrected experimental cross sections and $\delta\sigma_j$ are the associated uncertainties. The integrated cross sections $d\sigma(x_j)_{\text{int}}/d\Omega$ were defined by

$$\frac{d\sigma(x_j)_{\text{int}}}{d\Omega}=\frac{\int \exp\left[-\frac{(x-\mu_j)^2}{2\Delta_j^2}\right]\frac{d\sigma(x)}{d\Omega}dx}{\int \exp\left[-\frac{(x-\mu_j)^2}{2\Delta_j^2}\right]dx} , \tag{5}$$

where μ_j and Δ_j are the mean and the standard deviation, respectively, of the acceptance distribution of the jth pion array. The integration was done numerically over an interval of $\mu_j\pm5\Delta_j$. The finite-acceptance correction for the jth pion array, $C_{\text{FA}j}$, was then calculated using

$$C_{\text{FA}j}=\frac{\frac{d\sigma(x_j)}{d\Omega}}{\frac{d\sigma(x_j)_{\text{expt}}}{d\Omega}} . \tag{6}$$

This correction was normally less than 1%, but was on the order of a few percent where the dip of the angular distribution was steepest at the higher momenta. The largest correction was 5.9% for counter 5 ($\cos\theta=-0.289$) at 687 MeV/c π^-.

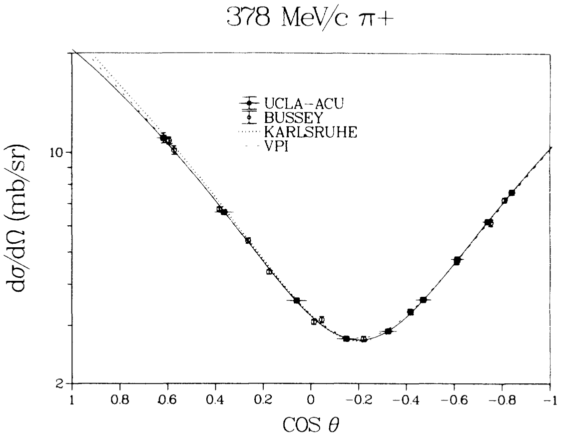

FIG. 2. Angular distribution for 378 MeV/c π^+.

IV. RESULTS

A. Tabulation

The differential cross sections are given in Tables III and IV for π^+ and π^-, respectively. These results replace the preliminary data published earlier.[25] The first row gives the laboratory momentum and kinetic energy and the overall normalization uncertainty for a given data set. The 687-MeV/c π^+ data were normalized to the Karlsruhe-Helsinki[26,27] partial-wave analysis because of the large proton contamination of the incident beam. The $\cos\theta$ and $\Delta(\cos\theta)$ that are listed are the means μ_j and standard deviations Δ_j of the acceptance distributions discussed in the previous section. The observed differential cross sections, listed in column 3, include the Monte Carlo corrections and the finite-acceptance corrections ($C_{\text{FA}j}$) which were discussed in the previous section. The electromagnetic corrections, C_{EM} which have been applied to the data are listed in column 4. C_{EM} corrects for

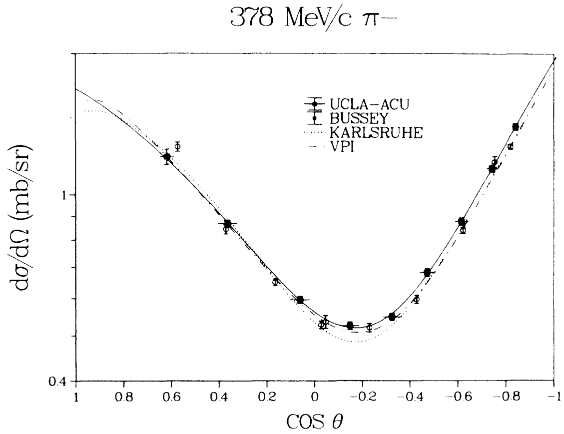

FIG. 3. Angular distribution for 378 MeV/c π^-.

TABLE III. π^+p elastic differential cross sections. All cross sections, electromagnetic corrections, and uncertainties are given in mb/sr.

$\cos\theta$	$\Delta(\cos\theta)$	$\frac{d\sigma_{\mathrm{expt}}}{d\Omega}$	C_{EM}	$\frac{d\sigma_{\mathrm{cor}}}{d\Omega}$	Uncertainty
Momentum = 378.0 MeV/c, kinetic energy = 263.4 MeV, normalization uncertainty = 3.1%.					
0.617	0.030	11.16	−0.11	11.05	0.38
0.363	0.042	6.621	−0.027	6.594	0.099
0.059	0.044	3.574	−0.001	3.572	0.059
−0.149	0.043	2.726	0.006	2.732	0.047
−0.324	0.039	2.874	0.010	2.884	0.050
−0.471	0.035	3.577	0.014	3.591	0.064
−0.614	0.029	4.749	0.018	4.767	0.083
−0.742	0.023	6.17	0.02	6.19	0.10
−0.842	0.016	7.57	0.02	7.59	0.12
Momentum = 407.9 MeV/c, kinetic energy = 291.5 MeV, normalization uncertainty = 4.1%.					
0.800	0.013	12.93	−0.27	12.65	0.40
0.607	0.031	9.23	−0.06	9.17	0.23
0.350	0.043	5.335	−0.003	5.332	0.064
0.044	0.044	2.643	0.009	2.652	0.035
−0.164	0.042	1.866	0.013	1.880	0.026
−0.338	0.038	1.832	0.018	1.850	0.026
−0.483	0.034	2.304	0.024	2.328	0.033
−0.624	0.028	3.125	0.031	3.157	0.044
−0.749	0.022	4.066	0.040	4.106	0.054
−0.846	0.016	5.105	0.047	5.152	0.067
Momentum = 427.4 MeV/c, kinetic energy = 310.0 MeV, normalization uncertainty = 2.1%.					
0.796	0.013	10.87	−0.22	10.65	0.42
0.601	0.031	7.52	−0.03	7.49	0.13
0.342	0.043	4.429	0.008	4.437	0.060
0.034	0.044	2.035	0.013	2.048	0.030
−0.173	0.042	1.360	0.016	1.376	0.021
−0.346	0.038	1.286	0.020	1.306	0.021
−0.491	0.033	1.649	0.027	1.676	0.027
−0.630	0.028	2.224	0.035	2.259	0.034
−0.753	0.021	2.938	0.045	2.983	0.044
−0.849	0.016	3.747	0.053	3.800	0.053
Momentum = 470.9 MeV/c, kinetic energy = 351.6 MeV, normalization uncertainty = 3.6%.					
0.788	0.014	8.08	−0.15	7.93	0.31
0.586	0.034	5.73	−0.01	5.72	0.10
0.321	0.043	3.187	0.016	3.203	0.042
0.012	0.044	1.334	0.012	1.346	0.018
−0.195	0.041	0.738	0.011	0.749	0.012
−0.365	0.037	0.656	0.014	0.670	0.011
−0.507	0.032	0.839	0.019	0.858	0.014
−0.643	0.027	1.213	0.027	1.239	0.020
−0.762	0.020	1.629	0.036	1.665	0.025
−0.855	0.015	2.104	0.044	2.148	0.031
Momentum = 509.0 MeV/c, kinetic energy = 388.2 MeV, normalization uncertainty = 3.5%.					
0.781	0.013	6.64	−0.21	6.43	0.25
0.574	0.031	4.490	−0.065	4.424	0.057
0.306	0.044	2.553	−0.018	2.534	0.034
−0.006	0.044	0.943	−0.003	0.940	0.012
−0.212	0.041	0.4529	0.0003	0.4532	0.0070

TABLE III. (*Continued*).

$\cos\theta$	$\Delta(\cos\theta)$	$\frac{d\sigma_{\mathrm{expt}}}{d\Omega}$	C_{EM}	$\frac{d\sigma_{\mathrm{cor}}}{d\Omega}$	Uncertainty
−0.381	0.036	0.3437	0.0015	0.3452	0.0061
−0.521	0.032	0.4591	0.0020	0.4611	0.0079
−0.654	0.026	0.681	0.002	0.683	0.011
−0.770	0.020	0.974	0.002	0.977	0.015
−0.860	0.014	1.264	0.002	1.266	0.018
Momentum = 547.0 MeV/c, kinetic energy = 425.0 MeV, normalization uncertainty = 2.1%.					
0.774	0.014	5.64	−0.17	5.47	0.22
0.562	0.033	3.725	−0.053	3.672	0.051
0.289	0.044	1.954	−0.015	1.939	0.030
−0.024	0.044	0.682	−0.003	0.680	0.012
−0.229	0.041	0.2741	0.0000	0.2741	0.0075
−0.396	0.036	0.1801	0.0009	0.1810	0.0069
−0.534	0.031	0.2634	0.0012	0.2646	0.0093
−0.664	0.025	0.412	0.001	0.414	0.012
−0.777	0.019	0.582	0.001	0.583	0.015
−0.864	0.014	0.747	0.001	0.749	0.016
Momentum = 586.0 MeV/c, kinetic energy = 462.8 MeV, normalization uncertainty = 2.4%.					
0.766	0.014	4.63	−0.14	4.50	0.12
0.548	0.039	2.988	−0.042	2.946	0.041
0.272	0.044	1.575	−0.012	1.563	0.024
−0.042	0.043	0.5012	−0.0022	0.4990	0.0076
−0.246	0.040	0.1615	−0.0002	0.1613	0.0051
−0.411	0.035	0.0811	0.0005	0.0816	0.0042
−0.546	0.030	0.1374	0.0008	0.1382	0.0062
−0.673	0.024	0.2142	0.0009	0.2151	0.0066
−0.784	0.018	0.3437	0.0009	0.3446	0.0086
−0.869	0.014	0.4300	0.0009	0.4309	0.0095
Momentum = 625.0 MeV/c, kinetic energy = 500.8 MeV, normalization uncertainty = 2.6%.					
0.759	0.014	3.56	−0.11	3.44	0.11
0.538	0.040	2.469	−0.035	2.434	0.031
0.258	0.044	1.236	−0.010	1.226	0.017
−0.058	0.043	0.3563	−0.0018	0.3545	0.0063
−0.261	0.040	0.0851	−0.0003	0.0848	0.0044
−0.425	0.035	0.0401	0.0002	0.0403	0.0053
−0.559	0.030	0.0652	0.0004	0.0656	0.0073
−0.683	0.024	0.140	0.001	0.141	0.010
−0.791	0.018	0.210	0.000	0.210	0.011
−0.873	0.013	0.254	0.000	0.254	0.010
Momentum = 657.0 MeV/c, kinetic energy = 532.1 MeV, normalization uncertainty = 5.0%.					
0.753	0.021	3.25	−0.10	3.15	0.12
0.527	0.041	2.244	−0.030	2.214	0.028
0.245	0.045	1.112	−0.008	1.104	0.015
0.072	0.043	0.2985	−0.0034	0.2951	0.0061
−0.274	0.039	0.0724	−0.0004	0.0720	0.0047
−0.436	0.034	0.0360	0.0000	0.0360	0.0057
−0.568	0.029	0.0634	0.0002	0.0636	0.0081
−0.690	0.023	0.131	0.000	0.131	0.011
−0.796	0.018	0.179	0.000	0.179	0.012
−0.876	0.013	0.190	0.000	0.190	0.012

TABLE III. (*Continued*).

$\cos\theta$	$\Delta(\cos\theta)$	$\frac{d\sigma_{\text{expt}}}{d\Omega}$	C_{EM}	$\frac{d\sigma_{\text{cor}}}{d\Omega}$	Uncertainty
Momentum = 687.0 MeV/c, kinetic energy = 561.5 MeV, normalization uncertainty = 15%.					
0.746	0.022	2.77	−0.08	2.69	0.11
0.517	0.042	1.872	−0.025	1.846	0.024
0.232	0.045	0.882	−0.007	0.875	0.012
−0.085	0.043	0.2252	−0.0014	0.2238	0.0041
−0.286	0.039	0.0525	−0.0004	0.0521	0.0026
−0.447	0.034	0.0352	−0.0001	0.0351	0.0026
−0.576	0.029	0.0759	0.0000	0.0759	0.0040
−0.696	0.023	0.1180	0.0001	0.1181	0.0048
−0.800	0.017	0.1429	0.0001	0.1430	0.0053
−0.879	0.012	0.1330	0.0001	0.1331	0.0051

Coulomb scattering and Coulomb-nuclear interference and was calculated using computer routines supplied by the Karlsruhe-Helsinki group. Various groups incorporate the electromagnetic corrections differently, so they are listed separately. The corrected differential cross sections are listed in column 5. The overall relative uncertainties are listed in the last column.

B. Comparison to existing data and to partial-wave analyses

Selective plots of the differential cross sections (after electromagnetic corrections) as a function of $\cos\theta_{\text{c.m.}}$ are given in Figs. 2—15. The relative uncertainties from Tables III and IV are shown as vertical error bars. The horizontal bars indicate the standard deviations of the acceptance distributions discussed above. Also shown are results of the fits using Legendre expansions (solid curves), and predictions of the Karlsruhe[26,27] (dotted curves), CMU-LBL (Ref. 11) (dashed curves), and VPI (Ref. 28) (dot-dashed curves) partial-wave analyses (PWA's). The PWA's include electromagnetic effects since that is what is available from the computer program SAID (scattering analysis interactive dial in) made available at LAMPF by the VPI group. The VPI analysis includes preliminary results from this work. Data from previous experiments are included when there is a reasonable match in the momentum and when the data are comparable in quality to the present work, or when there are serious discrepancies with the present results. Comparisons with older data with large error bars, with data taken over a limited angular range, or with data taken at only a few momenta have been avoided. The reader is referred to the SAID (Ref. 28) program for an exhaustive compilation of all published data in this momentum interval.

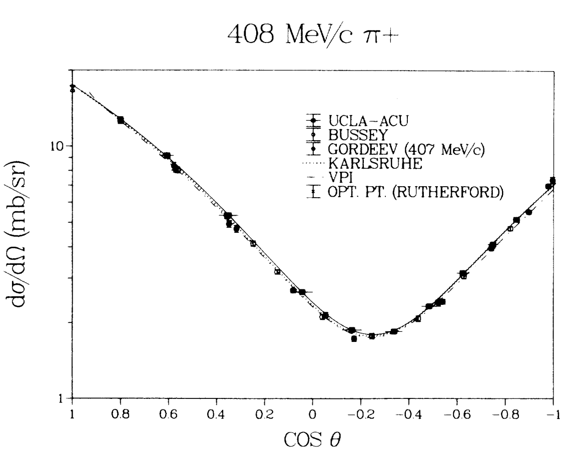

FIG. 4. Angular distribution for 408 MeV/c π^+.

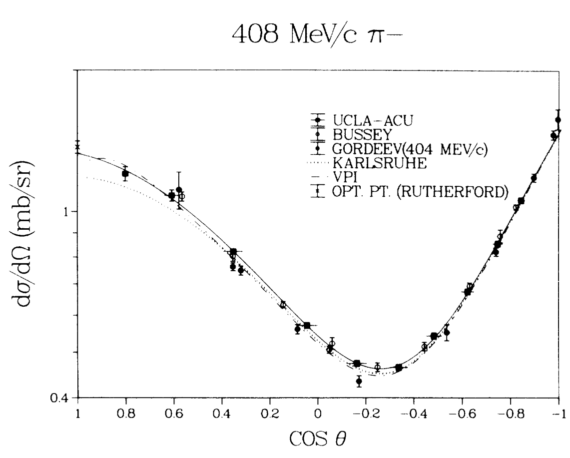

FIG. 5. Angular distribution for 408 MeV/c π^-.

TABLE IV. $\pi^- p$ elastic differential cross sections. All cross sections, electromagnetic corrections, and uncertainties are given in mb/sr.

$\cos\theta$	$\Delta(\cos\theta)$	$\frac{d\sigma_{\text{expt}}}{d\Omega}$	C_{EM}	$\frac{d\sigma_{\text{cor}}}{d\Omega}$	Uncertainty
Momentum = 378.0 MeV/c, kinetic energy = 263.4 MeV, normalization uncertainty = 5.0%.					
0.617	0.030	1.220	−0.003	1.217	0.045
0.363	0.042	0.878	−0.006	0.872	0.014
0.059	0.044	0.600	−0.002	0.598	0.010
−0.149	0.043	0.525	0.002	0.527	0.010
−0.324	0.039	0.546	0.004	0.550	0.010
−0.471	0.035	0.679	0.006	0.685	0.013
−0.614	0.029	0.874	0.008	0.882	0.016
−0.742	0.023	1.140	0.009	1.149	0.020
−0.842	0.016	1.400	0.010	1.410	0.024
Momentum = 407.9 MeV/c, kinetic energy = 291.5 MeV, normalization uncertainty = 2.9%.					
0.800	0.013	1.202	−0.002	1.200	0.042
0.607	0.031	1.082	−0.012	1.070	0.030
0.350	0.043	0.823	−0.009	0.815	0.011
0.044	0.044	0.5698	−0.0029	0.5669	0.0078
−0.164	0.042	0.4721	0.0005	0.4726	0.0072
−0.338	0.039	0.4621	0.0024	0.4645	0.0070
−0.483	0.034	0.5405	0.0032	0.5437	0.0084
−0.624	0.028	0.673	0.003	0.677	0.010
−0.749	0.022	0.854	0.003	0.857	0.013
−0.846	0.016	1.057	0.002	1.059	0.015
Momentum = 427.4 MeV/c, kinetic energy = 310.0 MeV, normalization uncertainty = 2.8%.					
0.796	0.013	1.070	−0.012	1.058	0.061
0.601	0.031	0.999	−0.015	0.984	0.042
0.342	0.043	0.783	−0.010	0.774	0.010
0.034	0.044	0.5211	−0.0024	0.5187	0.0068
−0.173	0.042	0.4182	0.0009	0.4191	0.0057
−0.346	0.038	0.3946	0.0021	0.3967	0.0056
−0.491	0.033	0.4528	0.0020	0.4548	0.0065
−0.630	0.028	0.5724	0.0009	0.5733	0.0084
−0.753	0.022	0.713	−0.001	0.712	0.010
−0.849	0.016	0.854	−0.003	0.851	0.012
Momentum = 470.9 MeV/c, kinetic energy = 351.6 MeV, normalization uncertainty = 2.1%.					
0.788	0.014	1.168	−0.032	1.136	0.048
0.586	0.033	1.083	−0.020	1.063	0.021
0.322	0.043	0.853	−0.011	0.843	0.011
0.012	0.044	0.5467	−0.0022	0.5445	0.0072
−0.194	0.041	0.4110	0.0010	0.4120	0.0057
−0.365	0.037	0.3627	0.0017	0.3644	0.0054
−0.508	0.032	0.3954	0.0009	0.3963	0.0062
−0.643	0.027	0.4906	−0.0011	0.4895	0.0079
−0.763	0.021	0.6189	−0.0039	0.6150	0.0092
−0.855	0.016	0.780	−0.007	0.774	0.011
Momentum = 509.0 MeV/c, kinetic energy = 388.2 MeV, normalization uncertainty = 2.5%.					
0.781	0.014	1.262	−0.017	1.245	0.055
0.573	0.038	1.131	−0.004	1.126	0.014
0.305	0.043	0.853	−0.002	0.851	0.011
−0.006	0.044	0.5073	−0.0019	0.5054	0.0068
−0.212	0.041	0.3516	−0.0020	0.3496	0.0050

TABLE IV. (*Continued*).

$\cos\theta$	$\Delta(\cos\theta)$	$\frac{d\sigma_{\text{expt}}}{d\Omega}$	C_{EM}	$\frac{d\sigma_{\text{cor}}}{d\Omega}$	Uncertainty
−0.381	0.036	0.3063	−0.0020	0.3043	0.0046
−0.521	0.032	0.3503	−0.0020	0.3483	0.0054
−0.653	0.026	0.4642	−0.0020	0.4622	0.0070
−0.770	0.020	0.6021	−0.0019	0.6002	0.0089
−0.860	0.015	0.759	−0.002	0.757	0.011
Momentum = 547.0 MeV/c, kinetic energy = 425.0 MeV, normalization uncertainty = 4.5%.					
0.774	0.014	1.487	−0.020	1.468	0.059
0.562	0.038	1.241	−0.004	1.237	0.017
0.290	0.044	0.879	−0.001	0.878	0.013
−0.024	0.044	0.4661	−0.0010	0.4651	0.0075
−0.229	0.041	0.3026	−0.0013	0.3013	0.0062
−0.396	0.036	0.2616	−0.0015	0.2601	0.0059
−0.534	0.031	0.3243	−0.0016	0.3227	0.0066
−0.664	0.025	0.485	−0.002	0.483	0.011
−0.778	0.019	0.647	−0.002	0.646	0.013
−0.865	0.014	0.844	−0.002	0.842	0.019
Momentum = 586.0 MeV/c, kinetic energy = 462.8 MeV, normalization uncertainty = 2.3%.					
0.764	0.015	1.883	−0.016	1.867	0.079
0.549	0.039	1.402	−0.001	1.401	0.016
0.273	0.044	0.924	−0.001	0.923	0.011
−0.042	0.044	0.4379	−0.0002	0.4377	0.0057
−0.246	0.040	0.2598	−0.0007	0.2591	0.0038
−0.411	0.035	0.2417	−0.0010	0.2407	0.0037
−0.546	0.030	0.3450	−0.0012	0.3438	0.0051
−0.673	0.024	0.5299	−0.0014	0.5285	0.0075
−0.784	0.018	0.751	−0.001	0.749	0.010
−0.869	0.013	1.010	−0.001	1.009	0.014
Momentum = 625.0 MeV/c, kinetic energy = 500.8 MeV, normalization uncertainty = 2.3%.					
0.760	0.015	2.077	−0.009	2.068	0.058
0.538	0.040	1.539	0.002	1.540	0.019
0.258	0.045	0.890	0.002	0.892	0.012
−0.058	0.043	0.3432	0.0005	0.3437	0.0054
−0.261	0.040	0.1696	−0.0002	0.1694	0.0039
−0.425	0.035	0.1943	−0.0007	0.1936	0.0051
−0.559	0.030	0.3179	−0.0010	0.3169	0.0077
−0.683	0.024	0.542	−0.001	0.541	0.011
−0.791	0.018	0.818	−0.001	0.816	0.017
−0.873	0.014	1.056	−0.001	1.055	0.019
Momentum = 657.0 MeV/c, kinetic energy = 532.1 MeV, normalization uncertainty = 2.2%.					
0.751	0.020	2.507	−0.006	2.501	0.091
0.526	0.041	1.722	0.003	1.726	0.022
0.243	0.045	0.900	0.003	0.903	0.012
−0.073	0.043	0.2945	0.0008	0.2953	0.0049
−0.274	0.039	0.1288	−0.0001	0.1287	0.0031
−0.436	0.034	0.1815	−0.0006	0.1809	0.0040
−0.568	0.029	0.3456	−0.0009	0.3447	0.0065
−0.690	0.023	0.614	−0.001	0.613	0.010
−0.796	0.018	0.907	−0.001	0.906	0.014
−0.876	0.013	1.218	−0.001	1.217	0.018

TABLE IV. (*Continued*).

$\cos\theta$	$\Delta(\cos\theta)$	$\frac{d\sigma_{\text{expt}}}{d\Omega}$	C_{EM}	$\frac{d\sigma_{\text{cor}}}{d\Omega}$	Uncertainty
Momentum = 687.0 MeV/c, kinetic energy = 561.5 MeV, normalization uncertainty = 2.3%.					
0.747	0.021	3.38	0.003	3.38	0.13
0.517	0.041	2.036	0.005	2.041	0.023
0.232	0.045	0.922	0.003	0.924	0.011
−0.085	0.043	0.2189	0.0006	0.2195	0.0040
−0.286	0.039	0.0870	−0.0002	0.0868	0.0030
−0.447	0.034	0.1877	−0.0007	0.1870	0.0040
−0.576	0.029	0.4065	−0.0009	0.4056	0.0074
−0.696	0.023	0.745	−0.001	0.744	0.012
−0.800	0.018	1.084	−0.001	1.083	0.016
−0.879	0.013	1.381	−0.001	1.380	0.019

Figure 2 shows the overall agreement with the results of Bussey *et al.*[29] for 378 MeV/c π^+. Figure 3 shows the data sets and PWA's for 378 MeV/c π^-. If a 2% renormalization is applied to either data set they agree very well except for their most forward angle. This point is the ostensible cause of the high value of χ^2 reported in their fit to these data. Our normalization uncertainty for the 378-MeV/c π^- data set is anomalously high (±5%) because of an inadvertent change in a channel-slit opening between the calibration runs and the production runs. This change in the beam phase space was observed to cause changes of a few percent in the calibration factor $F_C(r)$ discussed previously. The ionization chambers were used here for the calibration instead of the muon counters to obtain the number of beam particles.

The highest-momentum measurements of Bussey *et al.* are shown at 408 MeV/c in Fig. 4 (π^+) and Fig. 5 (π^-). The overall agreement is reasonably good, particularly at the back angles. Their data tend to be 1–2 % lower for the π^+, which is approximately the normalization uncertainty of either measurement. There is also good agreement with the PWA's, which is not surprising since they were heavily influenced by these data. The agreement with the measurements of Gordeev *et al.*[30] is not quite as good here. Their data are 3–4 % lower for the π^+ and 4–6 % lower for the π^- in the range $0.4 > \cos\theta > -0.6$. The large momentum bite could account for some of these discrepancies since their measurements had $\Delta p/p = 1.5\%$ (π^+) and 6.0% (π^-) compared to $\Delta p/p = 0.5\%$ for our measurements at this momentum (both π^+ and π^-). There are also slight (<1%) differences in the central beam momentum but they are in a direction which would produce an effect opposite to the discrepancies observed.

A comparison with the older data of Rugge and Vik[31] is shown in Fig. 7. These data differ from ours by ~20% at the forward angles and agree near $\cos\theta = -0.8$, even though the quoted relative uncertainties are ~2%. These results were routinely included in all but the most recent PWA's. As can be seen in Fig. 7, the data have a strong influence on the PWA's because of the large number of data points and the claim of small uncertainties. The data were not included in the VPI FP84 solution.

A comparison of the 687-MeV/c π^+ results with the 685-MeV/c results of Gordeev *et al.* is given in Fig. 14.

TABLE V. π^+ Legendre coefficients and total elastic cross sections.

P (MeV/c)	378	408	427	471	509
A_0 (mb/sr)	7.289±0.033	5.695±0.012	4.562±0.069	3.245±0.052	2.437±0.035
A_1 (mb/sr)	5.055±0.068	5.069±0.034	4.529±0.167	3.957±0.127	3.372±0.035
A_2 (mb/sr)	8.159±0.112	6.567±0.039	5.238±0.221	3.783±0.159	2.774±0.109
A_3 (mb/sr)	0.084±0.080	0.116±0.053	0.103±0.162	−0.013±0.114	−0.086±0.080
A_4 (mb/sr)			−0.118±0.118	−0.163±0.075	−0.213±0.050
χ_R^2	0.12	0.42	0.82	0.49	1.16
$\sigma_{\text{tot el}}$ (mb)	91.6±2.9	71.6±2.9	57.3±1.5	40.8±1.6	30.6±1.2
P (MeV/c)	547	586	625	657	687
A_0 (mb/sr)	1.969±0.033	1.578±0.024	1.253±0.021	1.171±0.024	0.971±0.019
A_1 (mb/sr)	3.051±0.083	2.622±0.059	2.168±0.053	2.025±0.059	1.723±0.046
A_2 (mb/sr)	2.306±0.105	1.808±0.073	1.392±0.067	1.208±0.073	1.060±0.055
A_3 (mb/sr)	0.039±0.078	0.010±0.054	−0.035±0.050	−0.096±0.054	−0.007±0.040
A_4 (mb/sr)	−0.197±0.049	−0.198±0.032	−0.233±0.031	−0.271±0.033	−0.259±0.021
χ_R^2	0.68	2.15	0.61	0.23	0.35
$\sigma_{\text{tot el}}$ (mb)	24.74±0.66	19.83±0.57	15.75±0.48	14.71±0.79	12.2±1.8

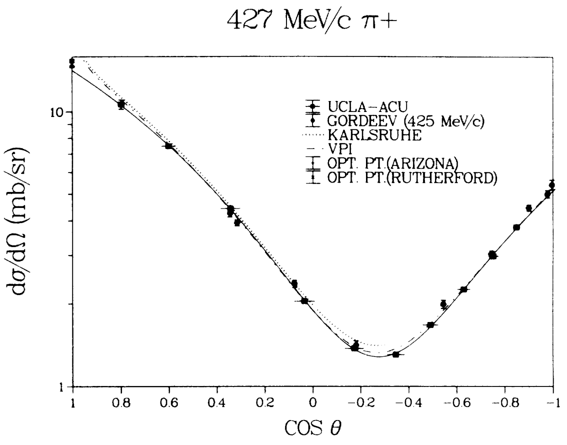

FIG. 6. Angular distribution for 427 MeV/c π^+.

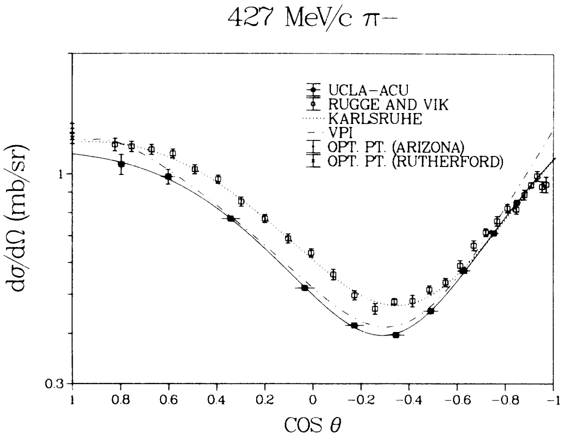

FIG. 7. Angular distribution for 427 MeV/c π^-.

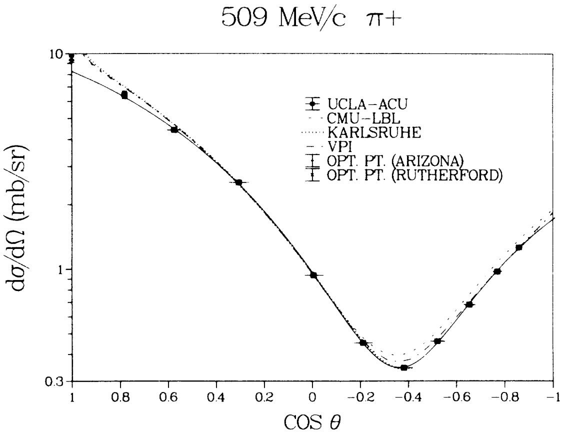

FIG. 8. Angular distribution for 509 MeV/c π^+.

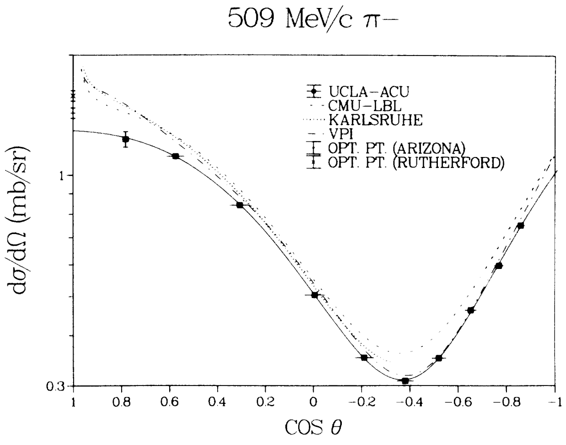

FIG. 9. Angular distribution for 509 MeV/c π^-.

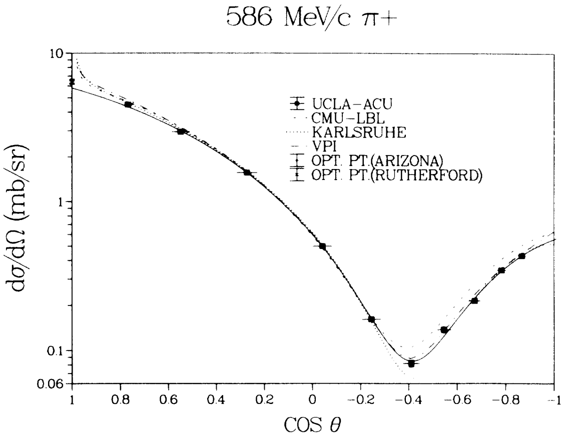

FIG. 10. Angular distribution for 586 MeV/c π^+.

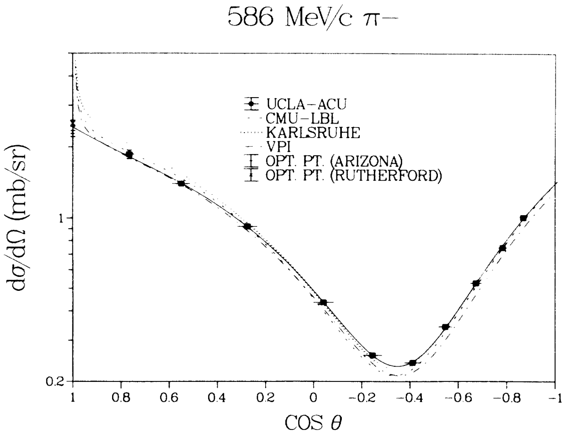

FIG. 11. Angular distribution for 586 MeV/c π^-.

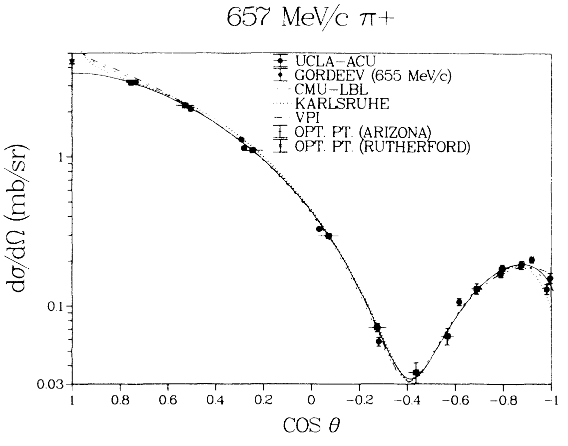

FIG. 12. Angular distribution for 657 MeV/c π^+.

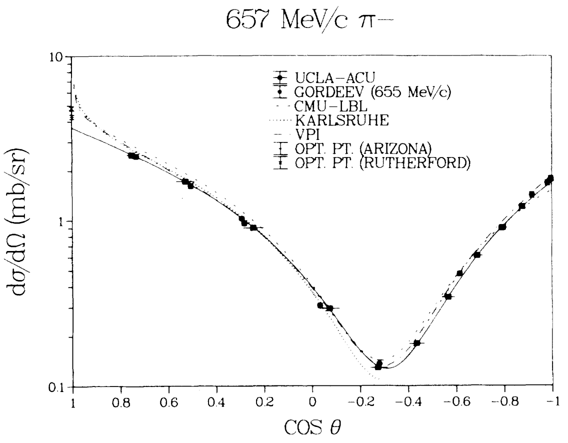

FIG. 13. Angular distribution for 657 MeV/c π^-.

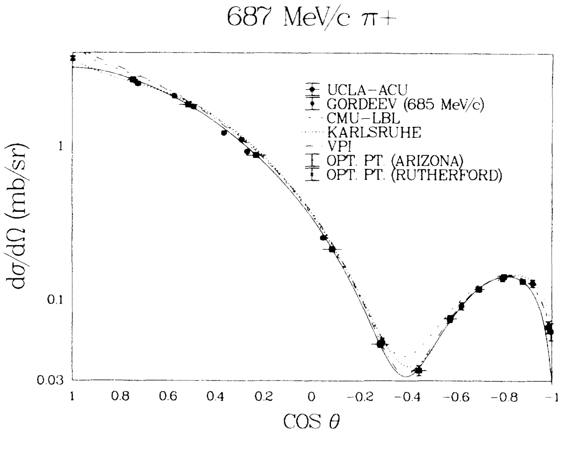

FIG. 14. Angular distribution for 687 MeV/c π^+.

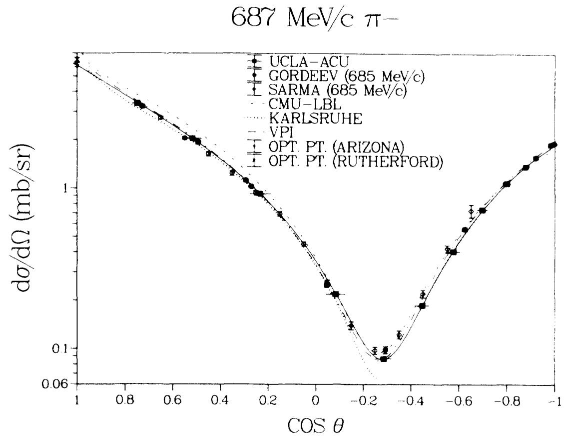

FIG. 15. Angular distribution for 687 MeV/c π^-.

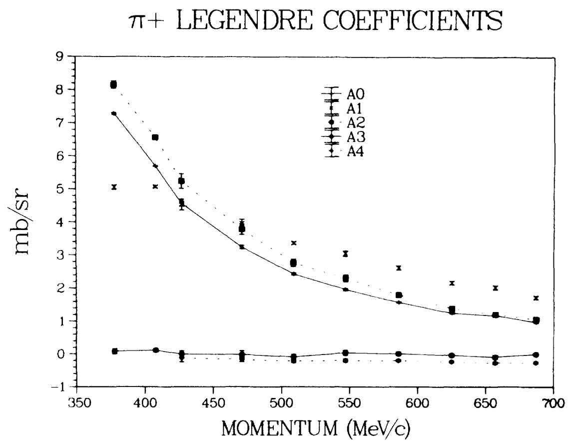

FIG. 16. Results of the fits to Legendre expansions as a function of π^+ beam momentum.

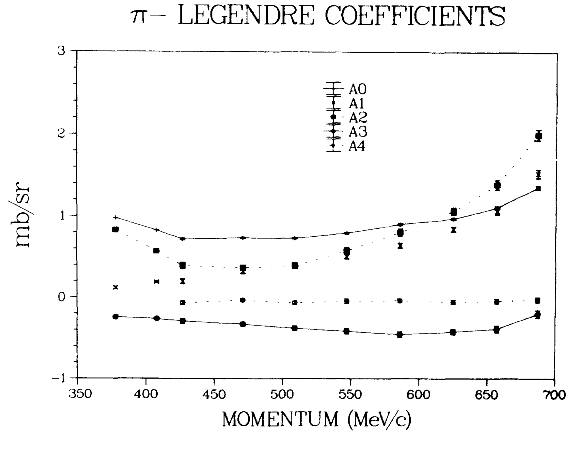

FIG. 17. Results of the fits to Legendre expansions as a function of π^- beam momentum.

TABLE VI. π^- Legendre coefficients and total elastic cross sections.

P (MeV/c)	378	408	427	471	509
A_0 (mb/sr)	0.978±0.001	0.829±0.001	0.716±0.013	0.732±0.010	0.728±0.010
A_1 (mb/sr)	0.118±0.017	0.190±0.010	0.195±0.031	0.321±0.033	0.381±0.024
A_2 (mb/sr)	0.831±0.001	0.570±0.001	0.390±0.040	0.363±0.033	0.394±0.035
A_3 (mb/sr)	−0.244±0.021	−0.261±0.014	−0.293±0.029	−0.330±0.026	−0.379±0.027
A_4 (mb/sr)			−0.067±0.023	−0.036±0.021	−0.065±0.021
$\chi_R{}^2$	0.32	0.36	0.65	0.34	0.68
$\sigma_{\text{tot el}}$ (mb)	12.29±0.61	10.41±0.30	9.00±0.30	9.20±0.23	9.15±0.26
P (MeV/c)	547	586	625	657	687
A_0 (mb/sr)	0.576±0.043	0.903±0.014	0.970±0.013	1.107±0.018	1.358±0.022
A_1 (mb/sr)	0.795±0.012	0.640±0.033	0.840±0.032	1.067±0.044	1.529±0.052
A_2 (mb/sr)	0.504±0.029	0.804±0.046	1.064±0.045	1.390±0.058	2.000±0.067
A_3 (mb/sr)	−0.415±0.033	−0.455±0.034	−0.422±0.033	−0.386±0.042	−0.203±0.047
A_4 (mb/sr)	−0.044±0.027	−0.040±0.024	−0.055±0.025	−0.044±0.028	−0.026±0.030
$\chi_R{}^2$	1.15	2.23	0.85	1.38	2.36
$\sigma_{\text{tot el}}$ (mb)	9.99±0.48	11.34±0.31	12.19±0.32	13.92±0.38	17.07±0.47

The agreement is excellent in shape. The present data provide a better description of the dip near $\cos\theta = -0.4$ while the Gordeev data extend farther backward in angle. The data of Sarma *et al.*[32] are also included in the π^- comparisons in Fig. 15. These data agree very well with each of the other data sets at the forward angles and are nominally 1—2 standard deviations high at the back angles. The measurement in the dip near $\cos\theta = -0.3$ is where the finite-acceptance correction was the largest for the present data (5.9%). Without this correction all three data sets would overlap.

After the electromagnetic corrections were applied to the data, each angular distribution was fitted to a Legendre expansion of the form

$$\frac{d\sigma}{d\Omega} = \sum_{i=0}^{n} A_i P_i(\cos\theta_{\text{c.m.}}) , \tag{7}$$

where the A_i are the fitted coefficients and the $P_i(\cos\theta_{\text{c.m.}})$ are the Legendre polynomials. The A_i are given in Tables V and VI and are plotted as a function of momentum in Figs. 16 and 17 for π^+ and π^-, respectively. The uncertainties are the diagonal elements of the error matrix for the fits and do not include the normalization uncertainties. The curves are drawn point to point without any smoothing. The number (n) of coefficients was chosen to give the minimum value of $\chi_R{}^2$ (the reduced χ^2 per degree of freedom). The exception to this rule was that fourth-order fits were always used above 427 MeV/c even though third-order fits gave a slightly smaller value $\chi_R{}^2$ for an occasional data set. Also, fifth-order fits yielded slightly lower $\chi_R{}^2$ for 657 and 687 MeV/c π^-, even though the values for A_5 were consistent with zero.

The total elastic cross sections were obtained from the Legendre fits using $\sigma_{\text{tot el}} = 4\pi A_0$. The uncertainties are the uncertainty in A_0 added in quadrature with the normalization uncertainties from Tables III and IV. These results are plotted in Figs. 18 and 19 for π^+ and π^-, respectively, along with the results from Gordeev *et al.* and the PWA's. Very little disagreement exists for the π^+ data although the present results are approximately one

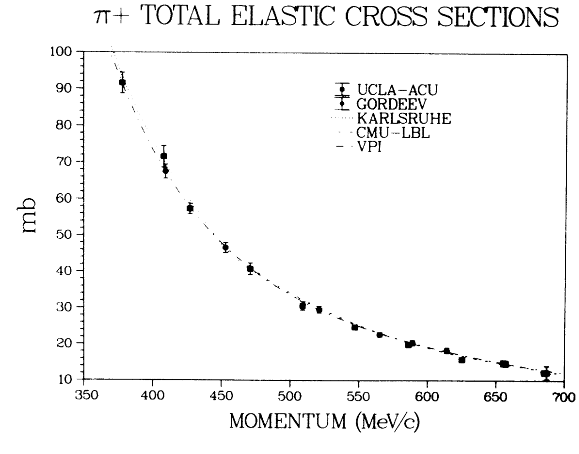

FIG. 18. Total π^+p elastic cross sections.

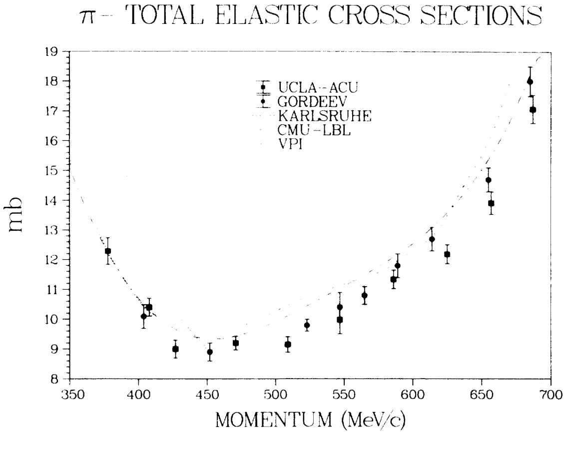

FIG. 19. Total π^-p elastic cross sections.

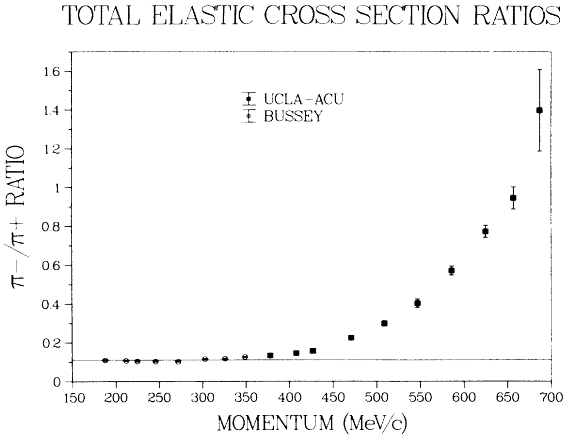

FIG. 20. Ratios of the π^- total elastic cross sections to that for π^+.

standard deviation lower than the consensus of the Gordeev data and the PWA's between 509 and 625 MeV/*c*. However, the present results are consistently one to two standard deviations lower than the PWA's for the π^- data (Fig. 19) at 427 MeV/*c* and above. The Gordeev results lie in between. This systematic offset between the two experiments arises from the inclusion of points at 0° by Gordeev *et al.* obtained by the Karlsruhe group using total cross section data and dispersion relations. These optical points were not used in the present fits because of the discrepancies between the Arizona[33] and Rutherford[34] groups in the measurements of the total cross sections. Furthermore, inclusion of the zero-degree cross sections based on either of these data sets had a deleterious effect on the value of $\chi_R{}^2$ which we obtained for the π^- data. The extension of our fitted angular distributions is consistently lower than the derived 0° cross sections as shown in Figs. 4—15.

The ratio of the π^- total elastic cross section to that for π^+ is shown in Fig. 20 as a function of momentum. The error bars reflect the uncertainties from Tables V and VI added in quadrature. The lower momentum points are derived from the data of Bussey *et al.*[29] after interpolating their π^- data to the momenta of their π^+ data. The solid line is drawn corresponding to a ratio of $\frac{1}{9}$, the expected value if the scattering is dominated by isospin $\frac{3}{2}$ amplitudes. The data reflect a smooth transition to the isospin $\frac{1}{2}$ resonance region, with no structure which might indicate a heretofore unreported narrow resonance.

ACKNOWLEDGMENTS

We acknowledge LAMPF's many contributions toward the successful completion of this experiment. We especially recognize A. Kirby and G. Suazo for their assistance in staging the experimental apparatus; J. Novak, N. Hoffman, and the cryogenics group for the design and implementation of the liquid-hydrogen target; and R. Macek and R. Werbeck for imparting their expertise on beam tuning in the P^3 channel. We appreciated the participation of M. Arman, F. Borcherding, P. Glodis, R. Haddock, N. Matz, and B. Silverman in the data-taking phase of the measurements. Students who contributed significantly in some phase of the data analysis were S. Adrain, M. Ballard, T. Black, K. Mitchell, A. Mokhtari, G. Olah, S. Shaffer, and M. Tate. We thank R. Arndt and L. Roper for useful discussions and for making the SAID program available which was used to produce the observables from the VPI and CMU-LBL analyses. We also thank G. Höhler, R. Koch, and M. Staudenmaier for their interaction and for making available their subroutines which produced the observables from the Karlsruhe analysis. This work was supported in part by the U.S. Department of Energy. One of us (M.E.S.) gratefully acknowledges the support of the Research Council of Abilene Christian University. W.J.B. and C.J.S. were supported in part by the George Washington University Committee on Research and by the National Science Foundation during the latter stages of analysis.

---

[*] Present address.

[†] Present address: Physics Department, George Washington University, Washington, DC 20052.

[‡] Present address: MS H838, Los Alamos National Laboratory, Los Alamos, New Mexico 87545.

[1] N. Isgur and G. Karl, Phys. Lett. **72B**, 109 (1977); Phys. Rev. D **19**, 2653 (1979).

[2] T. Barnes and F. E. Close, Phys. Lett. **116B**, 365 (1982); **123B**, 89 (1983).

[3] M. Karliner and M. P. Mattis, Phys. Rev. Lett. **56**, 428 (1986), and references therein.

[4] S. Weinberg, Trans. N.Y. Acad. Sci. **38**, 185 (1977).

[5] V. V. Abaev, V. S. Bekrenev, Yu. A. Beloglazov, V. G. Gaditsky, A. I. Kovalev, S. P. Kruglov, A. A. Kulbardis, I. V. Lopatin, A. N. Prokofiev, V. V. Sumachev, V. Yu. Trautman, E. P. Fedorova-Koval, E. A. Filimonov, and A. V. Shvedchikov, Z. Phys. A **311**, 217 (1983).

[6] M. E. Sadler, S. Adrain, F. O. Borcherding, W. J. Briscoe, A. Eichon, D. H. Fitzgerald, G. J. Kim, A. Mokhtari, B. M. K. Nefkens, G. Olah, C. J. Seftor, D. I. Sober, T. Walker, and J. A. Wightman, in *Proceedings of the Tenth International Union of Pure and Applied Physics Conference on Few Body Problems in Physics,* edited by B. Zeitnitz (North-Holland, Amsterdam, 1983), Vol. II, p. 217.

[7] M. Chanowitz and S. Sharpe, Nucl. Phys. **B222**, 211 (1983).

[8] T. Barnes and F. E. Close, Phys. Lett. **128B**, 277 (1983).

[9] E. Golowich, E. Haqq, and G. Karl, Phys. Rev. D **28**, 160 (1983).

[10] G. Höhler, in *Pion-Nucleon Scattering,* edited by H. Schopper (Springer, Berlin, 1983), Vol. I/9b2.

[11] R. E. Cutkosky, R. E. Hendrick, J. W. Alcock, Y. A. Chao, R. G. Lipes, J. C. Sandusky, and R. L. Kelly, Phys. Rev. D **20**, 2804 (1979); **20**, 2839 (1979); in *Baryon 1980,* proceedings of the IVth International Conference on Baryon Resonances, Toronto, edited by N. Isgur (University of Toronto, Toronto, 1981), p. 19.

[12]R. L. Crawford, in *Baryon 1980* (Ref. 11), p. 107.

[13]R. D. Baker, R. M. Brown, A. G. Clark, J. K. Davies, J. Depagter, W. M. Evans, R. J. Gray, E. S. Groves, R. J. Ott, T. P. Shah, A. J. Shave, J. J. Thresher, and M. W. Tyrrell, Nucl. Phys. **B156**, 93 (1979).

[14]R. Ayed, Report No. CEA-N-1921, 1976 (unpublished).

[15]V. V. Abaev, S. P. Kruglov, and Y. A. Malov, Leningrad Nuclear Physics Institute Report No. 438, 1978 (unpublished).

[16]R. A. Arndt, J. M. Ford, and L. D. Roper, Phys. Rev. D **32**, 1085 (1985).

[17]W. Celmaster, Phys. Rev. D **15**, 1391 (1977).

[18]B. Tatischeff, P. Berthet, M. P. Combes, J. P. Didelez, R. Frascaria, A. Boudard, J. M. Durand, M. Garcon, J. C. Lugol, Y. Terrien, R. Buertey, Y. Le Bornec, and L. Farvacque, Phys. Rev. Lett. **52**, 2022 (1984).

[19]R. D. Werbeck and R. J. Macek, IEEE Trans. Nucl. Sci. **NS-22**, 1598 (1975); J. Hudomalj, D. Mann, N. D. Gabitzsch, C. Bordner, and R. Macek, Nucl. Instrum. Methods **126**, 1 (1975); N. D. Gabitzsch, D. Mann, G. Pfeufer, G. C. Phillips, J. Hudomalj, L. Y. Lee, M. Warneke, J. C. Allred, R. J. Macek, and R. Werbeck, *ibid.* **126**, 7 (1975).

[20]D. Roeder and R. J. Macek, Los Alamos National Laboratory Report No. LA-7268-PR, 1977 (unpublished), pp. 31 and 32.

[21]W. J. Briscoe, D. H. Fitzgerald, B. M. K. Nefkens, and M. E. Sadler, Nucl. Instrum. Methods **197**, 277 (1982).

[22]K. L. Brown and Ch. Iselin, CERN Report No. 74-2, 1974 (unpublished).

[23]M. W. Tate and M. E. Sadler, Nucl. Instrum. Methods **204**, 295 (1983).

[24]R. E. Mischke and R. A. Williams, Los Alamos National Laboratory Report No. LA-UR-82-1952, 1982 (unpublished).

[25]M. E. Sadler, C. J. Seftor, F. O. Borcherding, W. J. Briscoe, D. H. Fitzgerald, P. F. Glodis, R. P. Haddock, and B. M. K. Nefkens, Phys. Lett. **119B**, 69 (1982).

[26]G. Höhler, F. Kaiser, R. Koch, and E. Pietarinen, *Handbook of Pion-Nucleon Scattering* (Physics Data No. 12-1) (Fachinformationszentrum, Karlsruhe, 1979).

[27]R. Koch and E. Pietarinen, Nucl. Phys. **A336**, 331 (1980).

[28]R. A. Arndt, L. D. Roper, and J. Ford, FP84 Analysis from the SAID computer program (unpublished). See also Ref. 16.

[29]P. J. Bussey, J. R. Carter, D. R. Dance, D. V. Bugg, A. A. Carter, and A. M. Smith, Nucl. Phys. **B58**, 363 (1973).

[30]V. A. Gordeev, V. P. Koptev, S. P. Kruglov, L. A. Kuz'min, A. A. Kulbardis, Yu. A. Malov, S. M. Mikirtich'yants, I. I. Strakovsky, and G. V. Scherbakov, Nucl. Phys. **A364**, 408 (1981).

[31]H. R. Rugge and O. T. Vik, Phys. Rev. **129**, 2300 (1963).

[32]H. N. K. Sarma, D. M. Binnie, J. Carr, N. C. Debenham, D. A. Garbutt, J. Keyne, P. Moissidis, and I. Siotis, Nucl. Phys. **B161**, 1 (1979).

[33]D. Davidson, T. Bowen, P. K. Caldwell, E. W. Jenkins, R. M. Kalbach, D. V. Peterson, A. E. Pifer, and R. E. Rothschild, Phys. Rev. D **6**, 1199 (1972).

[34]A. A. Carter, K. F. Riley, R. J. Tapper, D. V. Bugg, R. S. Gilmore, K. M, Knight, D. C. Salter, G. H. Stafford, J. D. Davies, J. D. Dowell, P. M. Hattersley, R. J. Homer, and A. W. O'Dell, Phys. Rev. **168**, 1457 (1968).